

# Ligand-Metal Charge Transfer Induced *via* Adjustment of Textural Properties Controls the Performance of Single-Atom Catalysts During Photocatalytic Degradation

Jiaxu Liu,<sup>‡[a,b]</sup> Yajun Zou,<sup>‡[c]</sup> Daniel Cruz,<sup>[d,e]</sup> Aleksandr Savateev,<sup>\*[c]</sup> Markus Antonietti,<sup>[c]</sup> and  
Gianvito Vilé<sup>\*[a]</sup>

<sup>[a]</sup> Department of Chemistry, Materials, and Chemical Engineering “Giulio Natta”, Politecnico di Milano, Piazza Leonardo da Vinci 32, 20133 Milan (Italy).

<sup>[b]</sup> State Key Laboratory of Fine Chemicals, Department of Catalytic Chemistry and Engineering, Dalian University of Technology, Ganjingzi District, Linggong Road 2, 116024 Dalian (China).

<sup>[c]</sup> Department of Colloid Chemistry, Max-Planck Institute of Colloids and Interfaces, Potsdam-Golm Science Park, Am Mühlenberg 1 OT Golm, 14476 Postdam (Germany).

<sup>[d]</sup> Fritz-Haber-Institut der Max-Planck-Gesellschaft, Faradayweg 4-6, 14195 Berlin (Germany).

<sup>[e]</sup> Department of Heterogeneous Reactions, Max Planck Institute for Chemical Energy Conversion, Mülheim an der Ruhr (Germany).

‡ These two authors contributed equally.

\*Corresponding authors. E-mails: [gianvito.vile@polimi.it](mailto:gianvito.vile@polimi.it) (G.V.)

[oleksandr.savatieiev@mpikg.mpg.de](mailto:oleksandr.savatieiev@mpikg.mpg.de) (A.S.)

## ABSTRACT

Because of their peculiar nitrogen-rich structure, carbon nitrides are convenient polydentate ligands for designing single-atom-dispersed photocatalysts. However, the relation between catalysts textural properties and their photophysical-photocatalytic properties is rarely elaborated. Herein we report the preparation and characterization of a series of single-atom heterogeneous catalysts featuring highly-dispersed Ag and Cu species on mesoporous graphitic C<sub>3</sub>N<sub>4</sub>. We show that adjustment of materials textural properties and thereby metal single-atom coordination mode enables ligand-to-metal (LMCT) or ligand-to-metal-to-ligand charge transfer (LMLCT), properties that were long speculated in single-atom catalysis, but never observed. We employ the developed materials in the degradation of organic pollutant under irradiation with visible light. Kinetic investigations under flow conditions show that single atoms of Ag and Cu decrease the amount of toxic organic fragmentation products, while leading to a higher selectivity towards full degradation. The results correlate with the selected mode of charge transfer in the designed photocatalysts and provide a new understanding of how the local environment of a single-atom catalyst affects surface structure and reactivity. The concepts can be exploited further to rationally design and optimize other single-atom materials.

**KEYWORDS:** Single-Atom Catalysis; Carbon Nitride; Ligand-to-Metal Charge Transfer; Catalytic Materials; Green Chemistry.

## 1. Introduction

Single-atom catalysts (SACs) have recently emerged as a new class of materials bridging the gap between the homogeneous and heterogeneous catalysis worlds.<sup>1-3</sup> These materials represent the utmost utilization of precious metals, while offering more facile preparation, handling, and recovery compared to traditional catalytic systems.<sup>4,5</sup> Due to the unsaturated coordination of the active center as well as quantum and support effects, over the past few years SACs were improved to show extraordinary catalytic activity and selectivity toward specific products in important transformations such as hydrogenation, oxidation, carbon-carbon coupling, water-gas-shift, and electrosynthesis.<sup>6-9</sup> Therefore, the scalable construction and application of SACs has emerged as a key topic important both for academic environment and for the industry.<sup>10-12</sup>

Deposition of stable single atoms on nitrogen-framed pores of carbon and carbon nitrides is perhaps the most successful strategy existing today to prepare SACs.<sup>13-15</sup> The polymeric semiconductor graphitic carbon nitride is, in fact, an optimal scaffold due to its nitrogen-rich structure (ideally,  $C_3N_4$ ), and the inherent nitrogen-lined pores can accommodate in a stable manner the metal species.<sup>16</sup> As such, it can facilitate stabilization of the metal single atoms *via* ‘strong metal-support interaction’ (SMSI).<sup>17,18</sup> Carbon nitrides and Ni-salts have been elegantly employed in photoredox catalysis.<sup>19-22</sup> At the same time, poly(heptazine imides) possessing alkali, alkaline earth abundant, and transition metal cations have been extensively studied in organic photoredox catalysis and  $H_2$  evolution.<sup>23-29</sup>

Typically, metal deposition is performed post-synthetically, by impregnation of prepared CN polymers with a metal salt, followed by metal reduction and/or thermal treatment.<sup>30</sup> However, this often leads to an undesirable decrease of the total surface area of the final composite compared to original material as well as potential metal clustering. An alternative approach to homogeneously introduce metals into the  $C_3N_4$  framework comprises the addition of a metal salt during the synthesis of carbon nitride. To avoid demixing, it has been shown that it is just crucial to select a suitable miscible and reactive metal precursor that would undergo co-condensation with the  $C_3N_4$  precursors in order to ensure homogeneity of the final composite.<sup>30</sup> Despite substantial efforts devoted to preparation of single atoms deposited into covalent  $C_3N_4$  framework

and their application in photocatalysis, structure-property-performance relationship is rarely elaborated. It is also unclear which properties make single-atom catalysts special.

From a practical standpoint, SACs can exhibit very sharp product selectivities, just as their homogeneous analogues. This makes them particularly suitable to overcome low selectivity patterns in many chemical transformations.<sup>31,32</sup> Among those, one of the most challenging remains the removal of leftover pharmaceutical contaminants from drinking water.<sup>33,34</sup> By using light and a photocatalyst, it is potentially possible to photo-oxidize organic pollutants to CO<sub>2</sub> and H<sub>2</sub>O. However, during degradation, stable product fragments that are more toxic than the initial substrate are frequently formed, limiting the industrial and societal exploitation of this technology.<sup>33</sup> For example, in the TiO<sub>2</sub>/Carbon dots-mediated photocatalytic degradation of Gemfibrozil (a drug used to cure abnormal blood lipid levels and found in drinking water), the contaminant easily degrades, but benzene derivatives are formed and released in the ‘purified’ water, creating acute toxicity.<sup>35,36</sup> Catalysts showing an increased selectivity towards CO<sub>2</sub> as a full Gemfibrozil degradation product and as a form of chemical (carbon) recovery have not been reported so far.<sup>37,38</sup>

In this work, we demonstrate that photocatalyst design involving atomically-dispersed metal species at mesoporous graphitic carbon nitride (mpg-C<sub>3</sub>N<sub>4</sub>) enables control and observation of ligand-metal charge transfer. In particular, using a series of spectroscopic techniques, we reveal that due to different coordination environment of metal single atoms on the surface of mpg-C<sub>3</sub>N<sub>4</sub> or in the bulk of the material, ligand-to-metal charge transfer (LMCT) or ligand-to-metal-to-ligand charge transfer (LMLCT) is operative. The selected mode of charge transfer determines the activity of the single-atom catalyst and, for the specific degradation of Gemfibrozil, it drives the selectivity towards enhanced formation of CO<sub>2</sub>. The results correlate with the selected mode of charge transfer in the designed single-atom materials and open new avenues for the understanding and rational design of single-atom photocatalysts.

## 2. Materials and Methods

**Catalyst Preparation.** Sodium tricyanomethanide (98%) was purchased from IoLiTec. AgNO<sub>3</sub> (≥99%), CuCl<sub>2</sub>·2H<sub>2</sub>O (≥99%), Cyanamide (99%), Ludox HS40 (40 wt.% suspension in water), NH<sub>4</sub>HF<sub>2</sub> (95%) were purchased from Sigma-Aldrich. The preparation of metal tricyanomethanides has been performed according to the modified procedure detailed below.

**Preparation of silver (I) tricyanomethanide.** A solution of AgNO<sub>3</sub> (1.70 g, 0.01 mol) in water (10 mL) was added in one portion to a stirred solution of sodium tricyanomethanide (1.13 g, 0.01 mol) in water (10 mL). The mixture was maintained at stirring in dark for 3 h. White solid was separated by centrifugation at 4000 rpm, washed with water (3×10 mL) and dried in vacuum (7 mbar, 50 °C). Yield: 1.92 g, 97%.

**Preparation of copper (II) tricyanomethanide.** A solution of CuCl<sub>2</sub>·2H<sub>2</sub>O (1.70 g, 0.01 mol) in water (10 mL) was added in one portion to a stirred solution of sodium tricyanomethanide (1.13 g, 0.01 mol) in water (10 mL). The mixture was maintained at stirring in dark for 3 h. White solid was separated by centrifugation at 4000 rpm, washed with water (3×10 mL) and dried in vacuum (7 mbar, 50 °C). Yield: 0.95 g, 39%.

**Synthesis of mpg-C<sub>3</sub>N<sub>4</sub> catalysts modified with Ag and Cu single atoms.** The synthesis of Ag@mpg-C<sub>3</sub>N<sub>4</sub> and Cu@mpg-C<sub>3</sub>N<sub>4</sub> has been performed according to the modified procedure.<sup>30</sup> Cyanamide (3.0 g), metal tricyanomethanide and a 40 % aqueous dispersion of 12 nm SiO<sub>2</sub> particles (Ludox HS40) (7.5 g) were mixed and heated at 70 °C under stirring for 16 h until water is completely evaporated. The resulting mixture was heated at a rate of 2.2 °C min<sup>-1</sup> over 4 h to reach a temperature of 550 °C and the temperature was kept for another 4 h. The resulting brown-yellow powder was briefly ground and treated with an NH<sub>4</sub>HF<sub>2</sub> solution (12 g in 50 mL of water) for 24 h to remove the silica template. The suspension was centrifuged and the precipitate was washed three times with distilled water and once with ethanol. Finally, the product was dried at 60 °C under vacuum overnight. For Ag1@mpg-C<sub>3</sub>N<sub>4</sub>, Ag2@mpg-C<sub>3</sub>N<sub>4</sub>, Cu1@mpg-C<sub>3</sub>N<sub>4</sub> and Cu2@mpg-C<sub>3</sub>N<sub>4</sub>, 30 mg (0.15 mmol) and 105 mg (0.53 mmol) of silver (I) tricyanomethanide, 37 mg (0.15 mmol) and 131 mg (0.53 mmol) of copper (II) tricyanomethanide were added, respectively. The mass of product obtained for Ag1@mpg-C<sub>3</sub>N<sub>4</sub>, Ag2@mpg-C<sub>3</sub>N<sub>4</sub>, Cu1@mpg-C<sub>3</sub>N<sub>4</sub> and Cu2@mpg-C<sub>3</sub>N<sub>4</sub> was 1.64 g, 1.35 g, 1.78 g and 1.61 g, respectively.

**Reference (transition metal free) mpg-C<sub>3</sub>N<sub>4</sub>.** The procedure of preparing mpg-C<sub>3</sub>N<sub>4</sub> was similar with that of Ag@mpg-C<sub>3</sub>N<sub>4</sub> and Cu@mpg-C<sub>3</sub>N<sub>4</sub> except that no metal tricyanomethanide was added. The mass of product obtained was 1.48 g.

**Catalyst characterization.** Scanning electron microscopy (SEM) and energy-dispersive X-ray (EDX) images were obtained on JSM-7500F (JEOL) at an accelerating voltage of 3 kV. EDX investigations were conducted using a Link ISIS-300 system (Oxford Microanalysis Group) equipped with a Si(Li) detector and an energy resolution of 133 eV. Transmission electron microscopy (TEM) study was performed using a double Cs corrected JEOL JEM-ARM200F (S)TEM operated at 80 kV equipped with a cold field emission gun. Powder X-ray diffractions (XRD) were recorded on Bruker D8 Advance diffractometer equipped with a scintillation counter detector with Cu K $\alpha$  radiation ( $\lambda = 0.15418$  nm). Elemental analysis was accomplished by combustion analysis using a Vario Micro device. Inductively Coupled Plasma Optical Emission spectroscopy (ICP-OES) study was performed using an Optima 8000 ICP-OES spectrometer (PerkinElmer). Nitrogen adsorption-desorption measurements were performed after degassing the samples at 150 °C for 20 hours using a Quantachrome Quadasorb SI-MP porosimeter at 77 K. The specific surface areas were calculated by applying the Brunauer-Emmett-Teller (BET) model to adsorption isotherms for  $0.05 < p/p_0 < 0.3$  using the QuadraWin 5.05 software package. The pore size distribution was obtained by applying the quenched solid density functional theory (QSDFT) model for N<sub>2</sub> adsorbed on carbon with cylindrical pore shape at 77 K. Optical absorbance spectra were measured on Shimadzu UV 2600 spectrophotometer equipped with an integrating sphere. Photoluminescence (PL) spectra were recorded and Quantum yield (QY) were measured using FP-8300 fluorescence spectrometer. Excitation wavelength was set to 365 nm. Time-resolved (TR)-PL spectra were recorded on fluorescence lifetime spectrometer (Fluo Time 250, PicoQuant) equipped with PDL 800-D picosecond pulsed diode laser drive. The decay curves were fitted using a nonlinear method with a multicomponent decay law given by the general formula  $I(t) = a_1 \exp(-t/\tau_1) + a_2 \exp(-t/\tau_2) + a_3 \exp(-t/\tau_3)$ . Electron paramagnetic resonance (EPR) study was conducted on Bruker EMXnano benchtop X-Band EPR spectrometer. The following settings were used: Center Field

3200 G, Sweep Width 3000 G, Receiver Gain 40 dB, Modulation Amplitude 1.000 G, Number of Scans 1, Microwave Attenuation 25 dB (0.3162 mW), room temperature. The Mott-Schottky measurements were carried out with Arbin electrochemical testing station (Arbin Instrument) in a standard three-electrode quartz cell. The working electrode was prepared as follows: 2 mg of sample was suspended in 0.2 mL of deionized water containing 0.02 mL of 5 wt.% Nafion D-520 dispersion, and the mixture was then dispersed by ultrasonication and spread onto an FTO glass. After being dried naturally, the FTO glass was heated at 120 °C for 1 h. The prepared thin film was employed as working electrode, with a platinum plate as counter electrode and Ag/AgCl as reference electrode (3M KCl). A 0.5 M Na<sub>2</sub>SO<sub>4</sub> aqueous solution was used as electrolyte (pH = 8.2). The measurement was carried out upon a frequency of 10 kHz in a potential range from -1.0 to 0.4 V vs. Ag/AgCl. The measured potentials vs. Ag/AgCl were converted to the reversible hydrogen electrode (RHE) scale according to the Nernst equation:  $E_{\text{RHE}} = E_{\text{Ag/AgCl}} + E^{\circ}_{\text{Ag/AgCl}} + 0.059 \text{ pH}$ , where  $E_{\text{RHE}}$  is the converted potential vs. RHE,  $E^{\circ}_{\text{Ag/AgCl}} = 0.1976$  at 25 °C, and  $E_{\text{Ag/AgCl}}$  is the experimentally measured potential against Ag/AgCl reference. X-Ray Photoelectron Spectroscopy (XPS) measurements were carried out with an X-ray gun Mg K $\alpha$  radiation (1254.6 eV) using CISSY end-station under ultra-high vacuum (UHV)  $1.5 \times 10^{-8}$  Pa, equipped with SPECS XR 50, and Combined Lens Analyzer Module (CLAM). The binding energy scale and Fermi level were calibrated using gold film. The XPS quantitative analysis were performed through CasaXPS software using Lorentzian-Gaussian functions and Shirley background deletion in photoemission spectra. Ultraviolet Photoelectron Spectroscopy (UPS) The UPS spectra were acquired with a He I (21.2 eV) radiation source. The detector was a Combined Lens with an analyzer module thermoVG (TLAM).

**Catalyst testing.** The photocatalytic performance of the prepared samples was studied using a solution of Gemfibrozil (10 mg) in deionized water (100 mL). This corresponds to a Gemfibrozil concentration of 100 ppm. All experiments were carried out using visible light (450 nm) irradiation. For the continuous-flow reactions, the water sample containing the pharmaceutical contaminant was pumped using a peristaltic pump through a custom-made photocatalytic reactor featuring a transparent column with a thin layer of

catalyst (100 mg, with 0.2-0.3 mm particles size). The LEDs extended vertically along each side of the reactor and illuminated the central manifold where the packed catalyst layer was present. The experimental conditions (temperature, pressure, and residence time) were varied to explore their effect on the pollutant degradation. For the case of batch experiments, Gemfibrozil (10 mg) and the catalyst (100 mg, nanopowder) were placed in deionized water (100 mL) and the suspension was placed into a round-bottom flask and irradiated using LED, placed along each side of the flask. The product solutions were analyzed by high-performance liquid chromatograph (Waters 1525 Binary HPLC pump). The stationary phase consisted in a Purospher Star RP-18 column (250 mm×4.6 mm, 5  $\mu$ m). The eluent phase was a mixture of water and methanol with a gradient concentration at a flow rate of 1.0 mL min<sup>-1</sup>. The concentration, conversion, and selectivity were calculated by peak area method. To determine the concentration of organic moiety in water, product solutions were also measured by elemental CHN analysis (2400 CHN, Perkin Elmer).

### 3. Results & Discussion

**Composition and textural characterization of the catalysts.** Traditional polymerization method yields g-C<sub>3</sub>N<sub>4</sub> with low surface area (below 10 m<sup>2</sup> g<sup>-1</sup>), resulting in limited activity in heterogeneous catalytic reactions.<sup>39</sup> Therefore, in this work, a ‘hard’ templating synthetic route using SiO<sub>2</sub> nanoparticles has been chosen as an effective technique to obtain ordered mesoporous structure. We have prepared, characterized, and evaluated a series of photocatalysts based on mpg-C<sub>3</sub>N<sub>4</sub>, containing isolated Ag and Cu single atoms on it. The introduction of silver and copper ions into a C<sub>3</sub>N<sub>4</sub> network has been accomplished by co-condensation of the respective tricyanomethanide salts with cyanamide in the presence of 12 nm SiO<sub>2</sub> nanoparticles as hard-template at 550 °C. During this process, the matrix nucleates and grows embedding into the template. Removal of the template by treatment with (NH<sub>4</sub>)HF<sub>2</sub> gives mesoporous structure of the material with high surface area, *i.e.* the template replica. The resultant mesostructured Ag/Cu mpg-C<sub>3</sub>N<sub>4</sub> with ordered porosity is expected to provide sufficient surface active sites and enhance light multi-reflection so as to enable efficient photocatalytic reactions. The final composition and textural properties of the reference and single-atom mesoporous graphitic carbon nitrides are shown in **Table 1**. Assuming ideal C<sub>3</sub>N<sub>4</sub>



molecular formula for the synthesized organic part of the material, the metal content in Ag@mpg-C<sub>3</sub>N<sub>4</sub>, *i.e.* 0.31-0.32 wt.%, suggests that statistically one silver atom is surrounded by *ca.* 100 heptazine units. In case of Cu@mpg-C<sub>3</sub>N<sub>4</sub>, the concentration of metal single atoms is higher, and for Cu1@mpg-C<sub>3</sub>N<sub>4</sub> it is one atom per 70 heptazine units, while for Cu2@mpg-C<sub>3</sub>N<sub>4</sub> it is one atom per 20 units. The percentage of metal transferred from the tricyanomethanide precursor into the material is higher for Cu (>79%) compared to Ag (7-32%). In particular, it is quantitative for Cu1@mpg-C<sub>3</sub>N<sub>4</sub> (**Table S2**). The mesoporous structure of the prepared materials is confirmed, independently from the presence of isolated metal species on it (**Table 1**).

**Table 1.** Elemental composition and textural properties of the reference mesoporous graphitic carbon nitride and single-atom-based catalysts.

Catalyst	C <sup>a</sup> [wt. %]	N <sup>a</sup> [wt. %]	H <sup>a</sup> [wt. %]	C/N [-]	Ag <sup>b</sup> [wt. %]	Cu <sup>b</sup> [wt. %]	S <sub>BET</sub> <sup>c</sup> [m <sup>2</sup> g <sup>-1</sup> ]	V <sub>pore</sub> <sup>d</sup> [cm <sup>3</sup> g <sup>-1</sup> ]
mpg-C <sub>3</sub> N <sub>4</sub>	31.90±0.12	48.75±0.39	2.43±0.04	0.65	-	-	157	0.46
Ag1@mpg-C <sub>3</sub> N <sub>4</sub>	30.08±0.46	47.31±0.08	2.61±0.02	0.64	0.32±0.02	-	127	0.25
Ag2@mpg-C <sub>3</sub> N <sub>4</sub>	31.37±0.01	47.37±0.08	2.30±0.02	0.66	0.31±0.02	-	232	0.60
Cu1@mpg-C <sub>3</sub> N <sub>4</sub>	31.58±0.02	49.05±0.04	2.47±0.02	0.64	-	0.54±0.01	274	0.72
Cu2@mpg-C <sub>3</sub> N <sub>4</sub>	32.27±0.18	47.96±0.18	2.33±0.04	0.67	-	1.66±0.03	257	0.71

<sup>a</sup>C, N, and H elemental analysis. Complete analysis is given in Table S1 in the Supporting Information. <sup>b</sup>ICP-OES data. <sup>c</sup>BET method applied to the N<sub>2</sub> isotherm collected at 77 K. <sup>d</sup>Quenched solid density functional theory model assuming cylindrical-shaped pores for the reference mpg-C<sub>3</sub>N<sub>4</sub> and single-atom catalysts.

The chemical structure of the final C<sub>3</sub>N<sub>4</sub>-based catalysts is similar to that of the reference mesoporous graphitic carbon nitride, as revealed by the X-ray diffraction patterns (**Figure 1a**). All mpg-C<sub>3</sub>N<sub>4</sub> samples have two characteristic diffraction peaks, at 13° and 27°. The former is related to an in-plane structural packing motif; the latter is attributed to the interplanar stacking of aromatic systems identified as the (002)

peak.<sup>40,41</sup> Single metal atoms disturb the local structure of C<sub>3</sub>N<sub>4</sub> network as illustrated by an intensity decrease and slight broadening of the stacking diffraction peak at 27° 2θ, suggesting an increased distortion of the stacking arrangement of the carbon nitride layers upon increase of the amount of Ag and Cu precursors.

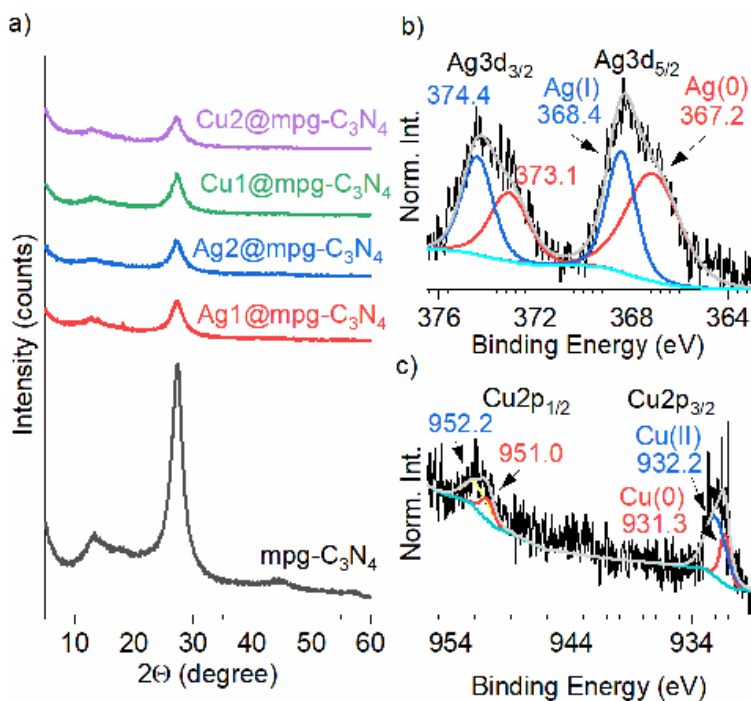


**Figure 1.** a) X-ray diffraction patterns of the different catalysts. b) Ag 3d XPS of Ag2@mpg-C<sub>3</sub>N<sub>4</sub>. c) Cu 3d XPS of Cu2@mpg-C<sub>3</sub>N<sub>4</sub>.

**Nature of the induced chemical changes in the C<sub>3</sub>N<sub>4</sub> network.** X-ray photoelectron spectroscopy (XPS) was performed followed by fitting with Lorentzian-Gaussian curves and analysis (**Figures S2-S3**). Quantitative analysis from XPS spectra reveals that the C/N atomic ratio of the samples is *ca.* 0.66 (**Table S3**), in line with the total C/N ratio. In XPS C 1s a peak at 284.0 eV (in literature mainly calibrated at 284.8 eV and defined as ‘adventitious carbon’)<sup>42</sup> we assign to electron rich, *e.g.* carbide-like, carbon (C<sub>carb</sub>).<sup>30</sup> The peak at 287.4 eV is assigned to carbon bound to terminal NH<sub>2</sub> groups (C–NH<sub>2</sub>). The peak at

288.7 eV is assigned to N–C=N moieties in heptazine rings.<sup>41</sup> The N 1s peak can be deconvoluted into three peaks centered at 398.8, 399.5 and 401.0 eV, corresponding to pyridinic N (C=N–C), tertiary nitrogen (N–(C)<sub>3</sub>), and amino functional groups (C–NH<sub>2</sub> and C–NH–C), respectively.<sup>43</sup> In general, introduction of either Ag or Cu single atoms leads to the shift of the C<sub>carb</sub> peak by 0.5–0.8 eV to higher energies,<sup>44</sup> indicating that metal single atoms bind selectively to electron rich sites in the carbon nitride and induce redistribution of electron density in the material.

XPS of Ag 3d exhibits peaks at 368.4 and 367.2 eV characteristic to Ag(I) and Ag(0) respectively (**Figure 1b**). Similarly, in XPS Cu 2p peaks at 932.2 and 931.3 eV are assigned to Cu(II) and Cu(0) respectively (**Figure 1c**). Presence of Ag(0) and Cu(0) peaks along with Ag(I) and Cu(II) complements XPS C 1s data and indicates partial charge transfer between carbon nitride framework and metal species. Indeed, it has been reported that Cu-single atoms deposited at carbon nitride<sup>45,46</sup> and graphene<sup>47,48</sup> carry partial positive charge. Based on integrated areas of the peaks, in Ag<sub>2</sub>@mpg-C<sub>3</sub>N<sub>4</sub> we estimate that 0.61e is transferred to silver (**Figure 1b**), while in Cu<sub>2</sub>@mpg-C<sub>3</sub>N<sub>4</sub>, 0.86e is transferred to copper (**Figure 1c**).

Morphology of the single-atom catalysts is similar to the reference mpg-C<sub>3</sub>N<sub>4</sub> and represented by particles with a diameter of *ca.* 20-200 nm as seen from the SEM images (**Figure S4**). TEM images show the presence of abundant mesopores, which originate from the removal of the template (**Figures S5**). These have an average pore size of *ca.* 5-15 nm, which is in line with the results of N<sub>2</sub> physisorption studies, showing type IV isotherms and type H3 hysteresis loops (**Figure S1**). The energy-dispersive X-ray spectra of all materials retrieved from the collected SEM and TEM maps confirm the presence of all relevant chemical elements (**Figures S6-S11**). High-angle annular dark-field scanning transmission electron microscopy (HAADF-STEM) investigation performed on an aberration-corrected microscope showed presence of silver and copper elements in an atomically dispersed form throughout the samples (**Figure 2**). The absence of any regions of higher local intensity can be confirmed in the Ag and Cu micrographs, verifying the absence of aggregated clusters and crystalline metal nanoparticles. Overall, the results of TEM study and XPS data point to the presence of an ensemble of Ag and Cu atoms in a fractional oxidation state,

which makes the prepared materials a joint electronic system modified with metal single atoms rather than isolated metal single sites only dropped onto a support. This confirms that the strong interaction between the support and metal sites is the key to the fabrication of single atoms catalyst and it is impossible to produce single atom catalysts by simply ‘dropping’ the metals on the cavities of the support.

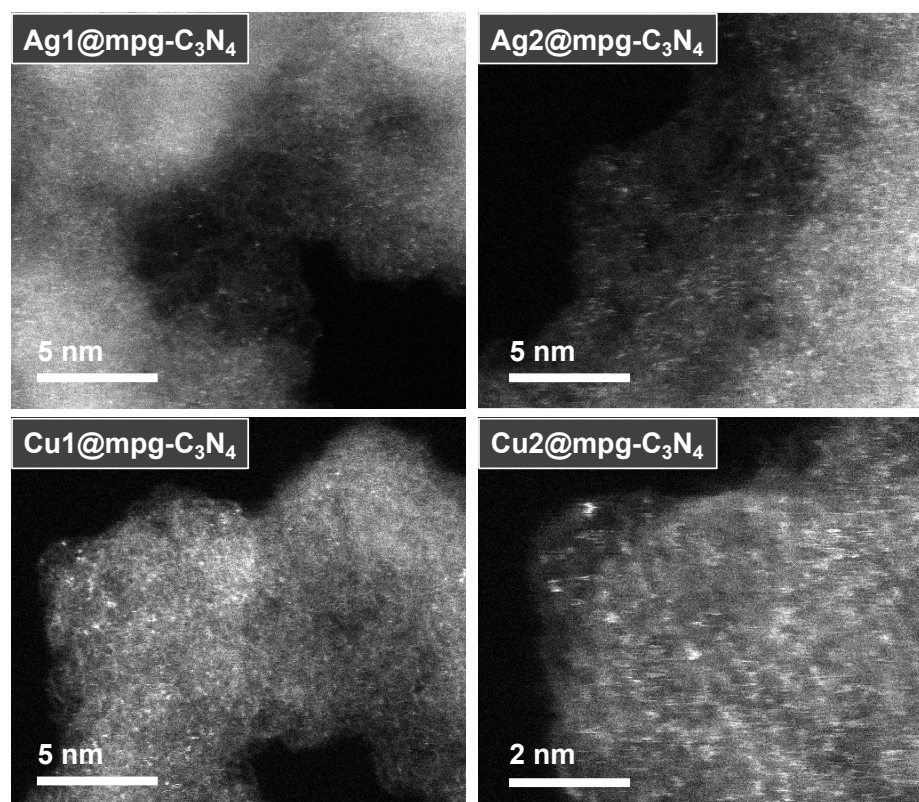


**Figure 2.** Aberration-corrected high resolution TEM images of the catalysts show isolated single atoms distributed across the mpg-C<sub>3</sub>N<sub>4</sub> support.

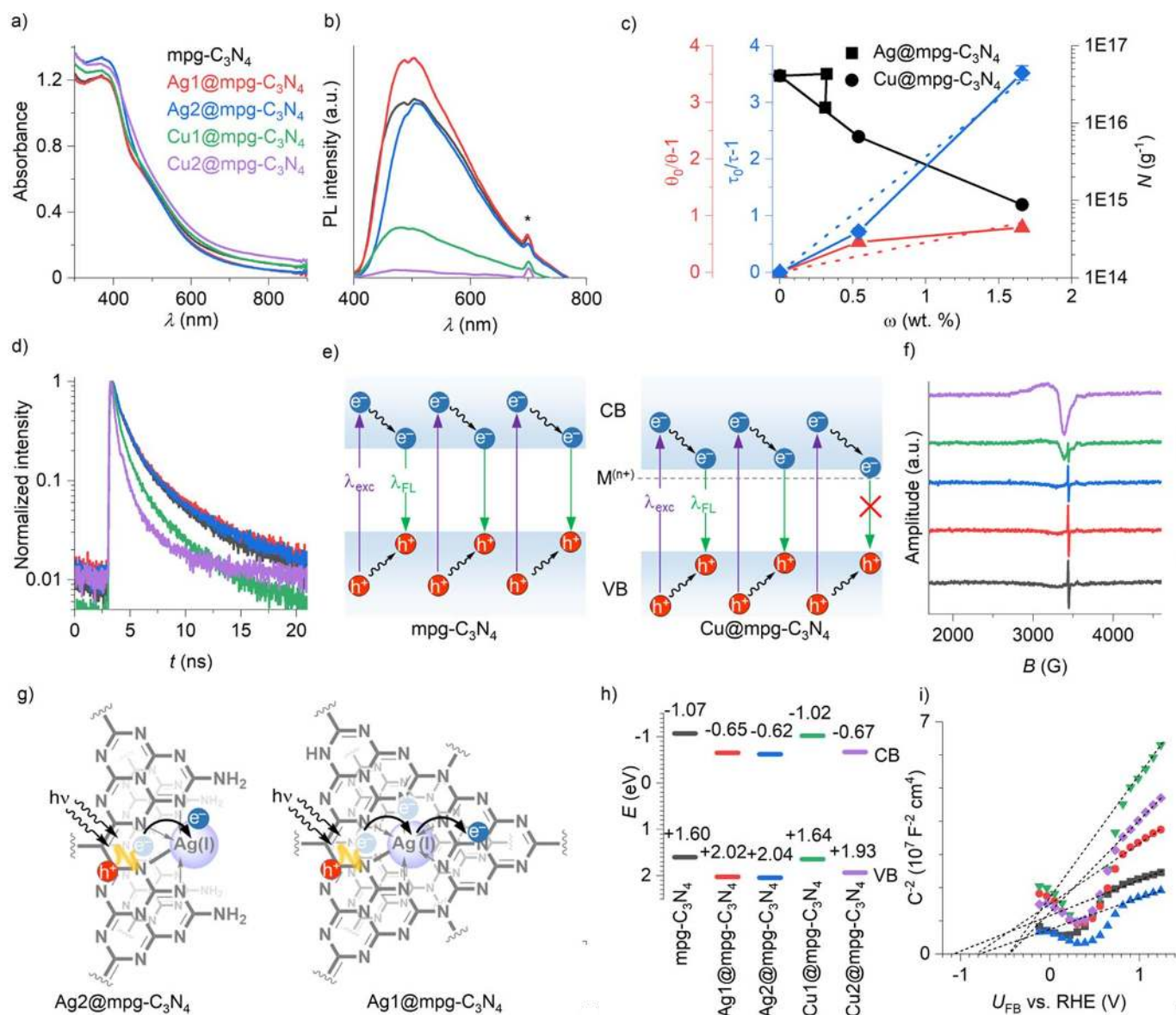


**Figure 3.** Characterization of materials. a) DRUV-vis absorption spectra. Color scheme is the same for the panels a),b),d),f),h) and i) shown in this Figure. b) Steady-state emission spectra of the materials recorded upon samples excitation with  $\lambda = 350$  nm. Asterisk denotes second order excitation light diffraction. c) Structure-property relationship shows dependence of physico-chemical properties of materials versus metal single atoms content. d) TRES upon samples excitation with  $\lambda = 375$  nm. e) Schematic representation of the effect of metal single atoms on band structure of the materials and excited state dynamics. Reference mpg-C<sub>3</sub>N<sub>4</sub> and Cu@mpg-C<sub>3</sub>N<sub>4</sub> are shown as examples. f) Room temperature X-band EPR spectra of materials in solid state. g) Schematic representation of LMCT in Ag<sub>2</sub>@mpg-C<sub>3</sub>N<sub>4</sub> and LLCT in Ag<sub>1</sub>@mpg-C<sub>3</sub>N<sub>4</sub>. h) Band structure of materials based on UPS and DRUV-vis absorption spectroscopy. i) Mott-Schottky plots.

The influence of metal single atoms on the electronic properties of the  $C_3N_4$  structure was first examined by diffuse reflectance UV-vis (DRUV-vis) absorption spectroscopy (**Figure 3a**). All samples absorb in the visible region of the electromagnetic spectrum. In particular, reference mpg- $C_3N_4$  shows an absorption edge at *ca.* 460 nm (equivalent to the absorption of photons with energy  $> 2.7$  eV), which originates from  $\pi-\pi^*$  transitions (**Figure 3a**).<sup>40,41</sup> Introduction of metal single atoms into the mpg- $C_3N_4$  has dual effect on light absorption properties of the material. Firstly, optical gap narrows by *ca.* 0.01-0.07 eV (**Figure S12**). This effect is most pronounced for Cu2@mpg- $C_3N_4$  and apparently due to the highest Cu content, 1.66 wt.%, in the studied series of materials. Secondly, light absorption in the range 500-800 nm is enhanced due to introduction of metal ions, which facilitate LMCT. Charge transfer between carbon nitride and metal atoms is further confirmed by quenching of mpg- $C_3N_4$  fluorescence (**Figure 3b**). The fluorescence internal quantum efficiency (IQE,  $\theta$ ) decreases from 0.65% for pristine mpg- $C_3N_4$  to 0.59% for Ag2@mpg- $C_3N_4$  and 0.36% for Cu2@mpg- $C_3N_4$  (**Table S4**). For comparative studies, we have selected materials modified with Cu because of similar textural properties, *i.e.* surface area and specific pore volume (**Table 1**), which eliminates influence of these parameters on photophysical properties (**Table 1**).<sup>49,50</sup> The influence of Cu single atoms on fluorescence quenching was quantitatively evaluated using the Stern-Volmer approach (**Figure 3c**). Thus, for Cu@mpg- $C_3N_4$  Stern-Volmer constant  $K_{SV}$  was calculated to be  $0.53$  (wt.%)<sup>-1</sup>.<sup>51</sup> The results of steady-state fluorescence quenching are supported by time-resolved emission spectra (TRES) (**Figure 3d, Table S5**). Thus, photogenerated charge carriers in Cu2@mpg- $C_3N_4$  have a *ca.* 5 times shorter lifetime compared to the reference mpg- $C_3N_4$ , namely  $172 \pm 3$  ps versus  $778 \pm 18$  ps. Fluorescence quenching rate constant  $k_q$  was calculated to be  $(2.63 \pm 0.06) \cdot 10^9$  (wt.%)<sup>-1</sup> s<sup>-1</sup>. Despite excitons in the reference mpg- $C_3N_4$  possess already very short lifetime compared, for example, to solutions of molecular photocatalysts,<sup>52</sup> introduction of Ag and Cu is still able to quench efficiently fluorescence, because single atoms are within subnanometer distance from the fluorophore, which facilitates their interaction, while diffusion as a potential rate limiting step is eliminated.<sup>53</sup> Taking into account low IQE for the set of the synthesized materials and TRES data, we conclude that excitons in mpg- $C_3N_4$  reach surface

states in less than 0.8 ns, while in Cu2@mpg-C<sub>3</sub>N<sub>4</sub> in less than 0.2 ns. In the notation adopted in semiconductor community, metal single atoms are considered as unoccupied defect states located close to the conduction band (CB) edge (**Figure 3e**).<sup>54</sup> In a studied series of materials, these surface states are non-fluorescent as seen from the steady-state emission spectra – no additional peaks are observed, while emission maxima are observed at *ca.* 500 nm (**Figure 3b**).

Electron paramagnetic resonance (EPR) spectroscopy was employed to probe the unpaired electrons in the catalysts (**Figure 3f**). The reference mpg-C<sub>3</sub>N<sub>4</sub> shows a sharp signal at 3440 G with *ca.* 5 G associated with the presence of radical species in the  $\pi$ -conjugated structure of the material. Introduction of metal single atoms leads to gradual quenching of the signal as the content of metal increases. Quantitative EPR reveals exponential decrease of the concentration of the radical species associated with the carbon nitride backbone (**Figure 3c**, **Table S6**). Materials with nearly identical textural properties, Ag2@mpg-C<sub>3</sub>N<sub>4</sub>, Cu1@mpg-C<sub>3</sub>N<sub>4</sub> and Cu2@mpg-C<sub>3</sub>N<sub>4</sub> (**Table 1**), show monotonous decrease of the specific concentration of radical species regardless of the incorporated metal ion (**Figure 3c**). At the same time, Ag1@mpg-C<sub>3</sub>N<sub>4</sub> having twice lower surface area and specific pore volume, but nearly the same content of Ag as Ag2@mpg-C<sub>3</sub>N<sub>4</sub>, falls out of this trend, implying that LMCT effectively proceeds only in case metal single atoms are localized at the surface of the material.<sup>55</sup> For the same reason, Ag1@mpg-C<sub>3</sub>N<sub>4</sub> shows even higher photoluminescence intensity (**Figure 3b**) and longer fluorescence lifetime compared to the reference mpg-C<sub>3</sub>N<sub>4</sub> (**Table S5**). For Cu@mpg-C<sub>3</sub>N<sub>4</sub> along with the quenching of the narrow signal, a broad peak covering the full spectral window evolves (**Figure 3f**). This signal is associated with Cu(II) paramagnetic centers, in agreement with the XPS data.<sup>56</sup>

Overall, spectroscopic data derived from steady-state emission spectroscopy, TRES and EPR spectroscopy strongly point to LMCT. This process occurs only in case of metal single atoms located at the surface of the material (**Figure 3g**). The possible reason consists in different coordination environment of surface metal single atoms and that located in the bulk of carbon nitride. Surface metal single atoms are coordinated by the carbon nitride from one side (a type of pincer complex), while in the bulk metal single atoms are entrapped into a cage created by heptazine units (cryptand-like complex). Therefore, for surface

metal single atoms only unidirectional electron transfer, from carbon nitride to the metal site, is possible. Contrary, bulk metal single atoms ‘conduct’ electrons via LMLCT.<sup>57,58</sup> Such charge transfer process in AgI@mpg-C<sub>3</sub>N<sub>4</sub> occurs on sub ps scale,<sup>59</sup> while enhanced electron mobility is registered as amplified EPR signal (**Table S6**), enhanced fluorescence (**Figure 3b**) and extended lifetime of the excitons (**Figure 3d**).

To investigate the influence of metal single atoms on the alignment of the energy levels, we determined the valence band (VB) energies using ultraviolet photoelectron spectroscopy (UPS) (**Figure S13**). Introduction of metal single atoms results in the shift of the VB by 0.04-0.45 eV to more positive numbers compared to pristine mpg-C<sub>3</sub>N<sub>4</sub> (**Figure 3h**). The influence is more pronounced for Ag@mpg-C<sub>3</sub>N<sub>4</sub> compared to Cu@mpg-C<sub>3</sub>N<sub>4</sub>. Subtraction of optical gap values derived from the Kubelka-Munk function from the VB energies gave CB energies of the materials, which are lower in energy compared to the reference mpg-C<sub>3</sub>N<sub>4</sub> (**Figure 3h**). We also applied the Mott-Schottky analysis to study the influence of metal single atoms onto quasi-Fermi level of electrons in the semiconductors (**Figure 3i**). All samples show a positive slope, which is characteristic for *n*-type semiconductors with electrons as major carriers. Flat band potential ( $U_{FB}$ ) of mpg-C<sub>3</sub>N<sub>4</sub> was determined to be -1.05 V *vs.* RHE, while for mpg-C<sub>3</sub>N<sub>4</sub> modified with Ag and Cu single atoms the corresponding  $U_{FB}$  values are shifted to more positive values, *i.e. ca.* -0.81 V and -0.46 V *vs.* RHE respectively (**Figure 3i**). Overall, our data indicates that LMCT and LMLCT arise from transfer of charges from the metal to the carbon nitride, which acts as ligand. This type of transfer is predominant in homogeneous complexes with relatively high energy lone pairs (*e.g.*, O, S or Se) or when the metal has low empty orbitals, but, to our knowledge, was never observed over single-atom catalysts.

**Charge transfer effects on the photocatalytic degradation of Gemfibrozil.** Using the materials described above, we have studied the photocatalytic removal of Gemfibrozil from deionized water. Gemfibrozil is a major contaminant present in drinking water samples and is among the emerging pollutants listed on the 3<sup>rd</sup> Watch List under the Water Framework Directive of the European Union.<sup>60</sup> This compound is hard to degrade using state-of-the-art technologies<sup>61</sup> and, when this happens, toxic organic moieties that are stable and soluble in water are formed.<sup>35,36</sup> Our catalytic tests have been conducted under continuous-



flow conditions. As shown in **Figure 4a**, the removal of Gemfibrozil increases with longer residence time ( $rt$ ) in the photoreactor, until reaching a plateau when  $rt > 25$  min. Such trend is common and has been reported elsewhere.<sup>62,63</sup> In fact, a heterogeneous photocatalytic reaction involves adsorption of reactants from a fluid phase onto a solid surface, surface reaction of the adsorbed species, and desorption of products into the fluid phase. Clearly, substances other than the reactants, including impurities, reaction intermediates, or (by)products, can also be adsorbed on the catalyst surface and inhibit the reaction due to partial occupation of the catalyst active sites, resulting in a decrease of the degradation rate. It is important to remark, however, that this effect is more visible over pristine mpg-C<sub>3</sub>N<sub>4</sub> and less over the single-atom catalysts.

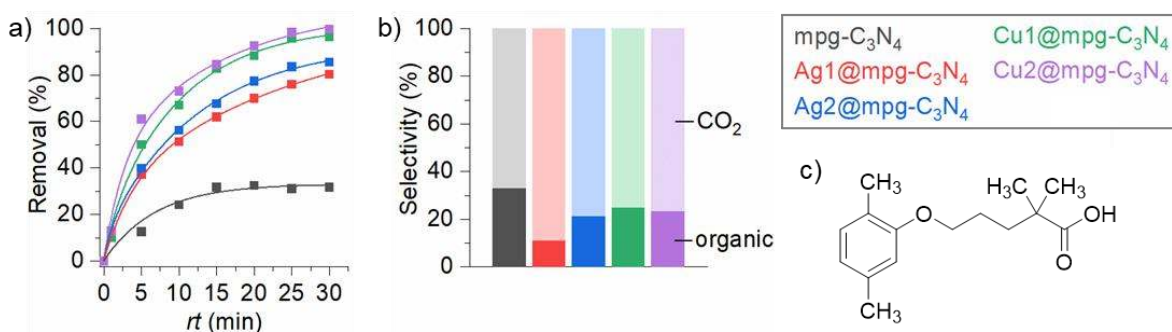


**Figure 4.** a) Influence of the photoreactor residence time ( $rt$ ) on the continuous-flow degradation of Gemfibrozil in water over pristine g-C<sub>3</sub>N<sub>4</sub> and metal-based single-atom catalysts. Conditions: [Gemfibrozil] = 100 ppm,  $m_{\text{cat}}$  = 100 mg, temperature = 30°C, pressure = 3 bar, light wavelength = 450 nm. b) Selectivity to CO<sub>2</sub> and amount of toxic organic byproducts over pristine mpg-C<sub>3</sub>N<sub>4</sub> and metal-based single-atom catalysts. Conditions: [Gemfibrozil] = 100 ppm,  $m_{\text{cat}}$  = 100 mg, temperature = 30°C, pressure = 3 bar,  $rt$  = 1-5 min (at a reference Gemfibrozil removal = 10%), light wavelength = 450 nm. c) Structure of Gemfibrozil.

The order of reactivity is Cu2@mpg-C<sub>3</sub>N<sub>4</sub> > Cu1@mpg-C<sub>3</sub>N<sub>4</sub> > Ag2@mpg-C<sub>3</sub>N<sub>4</sub> > Ag1@mpg-C<sub>3</sub>N<sub>4</sub> > mpg-C<sub>3</sub>N<sub>4</sub>. This effect does not change fixing the residence time, and varying the temperature or the

pressure (**Figure S14**), or using a slurry batch-type photoreactor (**Figure S15**). Also, the degradation takes place only in the presence of light, and a stable photocatalytic performance is observed for all materials (**Figure S16**).

Based on the data in **Figure 4a**, it is possible to model the photodegradation of Gemfibrozil in water, using the equation  $c = c_0 \exp(-kt)$ , where  $c$  represents the concentration of Gemfibrozil over time, and  $c_0$  is its initial concentration in water. This equation represents the best practice to simulate the photoreactor behaviour, considering that an in-depth analysis of Gemfibrozil degradation through *ab initio* simulations is not yet available. In particular, the equation corresponds to a pseudo first-order concentration decay, which is well applicable since the curves of  $\ln(c/c_0)$  versus retention time ( $rt$ ) show a nearly linear relationship (**Figure S17**). From this equation, the rate constant ( $k$ ) and estimated pollutant half-life ( $t_{1/2}$ ) have been determined (**Table S7**), to provide valuable kinetic insights. By comparing the rate constants with values available in the literature (**Table S8**), it is possible to appreciate that the efficiency of the single-atom materials. The estimated half-life for the contaminant degradation is in line with this result, and further demonstrates that Cu<sub>2</sub>@mpg-C<sub>3</sub>N<sub>4</sub> requires only 4 min to halve the contaminant concentration.

The photocatalytic performance can be correlated with the discussed above photophysical properties of the materials influenced by the introduction of single atoms (**Figure 3c**). Thus, fluorescence lifetime in combination with relatively low IQE (<1% for all materials studied herein) are seen as the parameters characterizing efficiency of charge separation and localization at non-radiative surface states. This process is the fastest for Cu<sub>2</sub>@mpg-C<sub>3</sub>N<sub>4</sub> ( $\tau = 172$  ps), which correlates with the highest activity in the degradation of Gemfibrozil. The nature of metal single atom has a clear influence on performance of the photocatalyst. Upon photoexcitation of Cu@mpg-C<sub>3</sub>N<sub>4</sub>, LMCT promotes reduction of Cu(II) to Cu(I)/Cu(0) mononuclear complexes. The latter activates oxygen via SET and therefore accelerates degradation of the pollutant.<sup>64,65,66</sup> Similar process in Ag@mpg-C<sub>3</sub>N<sub>4</sub> leads to the more stable Ag(0) species ( $E_{\text{Ag(I)}/\text{Ag(0)}} = +0.8$  V vs SHE). Therefore, metal single atoms not only adjust photophysical properties of the carbon nitride semiconductor but are efficiently involved in the process of Gemfibrozil degradation.

To unravel the product selectivity formed over the different photocatalysts, we have determined the organic content in the product solutions via CHN analysis (**Figure 4b**). Organic moieties, owing to the incomplete conversion of the Gemfibrozil core, are formed during the degradation. However, from the carbon balance, we estimate that a higher fraction of gaseous species and fewer organic byproducts are formed in case of using Ag@mpg-C<sub>3</sub>N<sub>4</sub> and Cu@mpg-C<sub>3</sub>N<sub>4</sub> compared to the reference mpg-C<sub>3</sub>N<sub>4</sub>. Ag1@mpg-C<sub>3</sub>N<sub>4</sub> clearly stands out as the most selective catalyst toward CO<sub>2</sub>, followed by Ag2@mpg-C<sub>3</sub>N<sub>4</sub>. Despite Cu2@mpg-C<sub>3</sub>N<sub>4</sub> showed the highest activity in removal of Gemfibrozil, its selectivity toward CO<sub>2</sub> is moderate, suggesting existence of follow up cascade, *i.e.* the drug molecule undergoes transformation quickly, but calcination is slower process. Note that the catalysts were compared at a similar degree of conversion and under kinetic conditions (10%). These results point that single-atom photocatalysts can reduce the amount of toxic species of benzene during the pollutant degradation. Although Ag1@mpg-C<sub>3</sub>N<sub>4</sub> and Ag2@mpg-C<sub>3</sub>N<sub>4</sub> have nearly the same Ag content, their textural properties are different (**Table 1**). As deduced from spectroscopic study bulk Ag single atoms in Ag1@mpg-C<sub>3</sub>N<sub>4</sub> facilitate electron transport that is beneficial to promote multistep pathway of Gemfibrozil degradation to CO<sub>2</sub>.

#### 4. Conclusions

We have prepared, characterized, and evaluated a series of single-atom heterogeneous catalysts featuring highly-dispersed metal species on mesoporous graphitic C<sub>3</sub>N<sub>4</sub>. Using this series of catalysts, we have shown that Ag and Cu single metal species can decrease the extent of aromatic byproducts and promote formation of CO<sub>2</sub>. By combining advanced characterization methods, we show that such results can be linked to ligand-metal charge transfer in the designed materials, as confirmed by DRUV-vis, TRES, fluorescence quantum efficiency, and EPR measurements. Specifically, textural properties of mpg-C<sub>3</sub>N<sub>4</sub> modified with metal single atoms influence the mode and type of charge transfer in the studied materials. This work not only shows the incorporation and use of Cu and Ag atoms on carbon nitride for photocatalytic water decontamination, but also opens fundamental directions in the design of selective photocatalysts for

advanced oxidation processes, showing how fine-tuning the band structure of the hybrid-semiconductor nanomaterials can lead to improved single-atom photocatalytic materials.

#### ASSOCIATED CONTENT

**Supporting Information.** Additional characterization data of the materials.

#### AUTHOR INFORMATION

##### **Corresponding Authors**

\*[gianvito.vile@polimi.it](mailto:gianvito.vile@polimi.it) (Dr. Gianvito Vilé)

\*[oleksandr.savatieiev@mpikg.mpg.de](mailto:oleksandr.savatieiev@mpikg.mpg.de) (Dr. Aleksandr Savateev)

##### **Author Contributions**

G.V. conceived the work. A.S. and G.V. coordinated the various stages of this research. Y.Z., D.C., J.L., and G.V. prepared and characterized the materials. The manuscript was written through contributions from all authors and everyone gave approval to the final version of the manuscript.

##### **Funding Sources**

G.V. thanks Fondazione Bracco and Fondazione Politecnico di Milano for funding.

##### **Conflicts of interest**

There are no conflicts to declare.

#### ACKNOWLEDGEMENTS

The authors thank Dr. Tobias Heil and Nadezda V. Tarakina (Max Planck Institute of Colloids and Interfaces) for TEM analysis, and Dr. Iver Laueremann (PVcomB staff) for facilitating the access to CISSY End Station at Helmholtz Zentrum Berlin.

## REFERENCES

- 1 Wang, A.; Li, J.; Zhang, T. Heterogeneous Single-Atom Catalysis. *Nat. Rev. Chem.* **2018**, *2*, 65-81.
- 2 Kaiser, S. K.; Chen, Z.; Faust Akl, D.; Mitchell, S.; Perez-Ramirez, J. Single-Atom Catalysts Across the Periodic Table. *Chem. Rev.* **2020**, *120*, 11703-11809.
- 3 Zhang, Z.; Chen, Y.; Zhou, L.; Chen, C.; Han, Z.; Zhang, B.; Wu, Q.; Yang, L.; Du, L.; Bu, Y.; Wang, P.; Wang, X.; Yang, H.; Hu, Z. The Simplest Construction of Single-Site Catalysts by the Synergism of Micropore Trapping and Nitrogen Anchoring. *Nat. Commun.* **2019**, *10*, 1657.
- 4 Liu, L.; Corma, A. Metal Catalysts for Heterogeneous Catalysis: From Single Atoms to Nanoclusters and Nanoparticles. *Chem. Rev.* **2018**, *118*, 4981-5079.
- 5 Ling, C.; Niu, X.; Li, Q.; Du, A.; Wang, J. Metal-Free Single Atom Catalyst for N<sub>2</sub> Fixation Driven by Visible Light. *J. Am. Chem. Soc.* **2018**, *140*, 14161-14168.
- 6 Vilé, G.; Albani, D.; Nachtegaal, M.; Chen, Z.; Dontsova, D.; Antonietti, M.; Lopez, N.; Perez-Ramirez, J. A Stable Single-Site Palladium Catalyst for Hydrogenations. *Angew. Chem. Int. Ed.* **2015**, *54*, 11265-11269.
- 7 Therrien, A. J.; Hensley, A. J. R.; Marcinkowski, M. D.; Zhang, R.; Lucci, F. R.; Coughlin, B.; Schilling, A. C.; McEwen, J.-S.; Sykes, E. C. H. An Atomic-Scale View of Single-Site Pt Catalysis for Low-Temperature CO Oxidation. *Nat. Catal.* **2018**, *1*, 192-198.
- 8 Chen, Z.; Vorobyeva, E.; Mitchell, S.; Fako, E.; Ortuno, M. A.; Lopez, N.; Collins, S. M.; Midgley, P. A.; Richard, S.; Vilé, G.; Perez-Ramirez, J. A Heterogeneous Single-Atom Palladium Catalyst Surpassing Homogeneous Systems for Suzuki Coupling. *Nat. Nanotechnol.* **2018**, *13*, 702-707.
- 9 Ju, W.; Bagger, A.; Wang, X.; Tsai, Y.; Luo, F.; Möller, T.; Wang, H.; Rossmeisl, J.; Varela, A. S.; Strasser, P. pH Effects on the Selectivity of the Electrocatalytic CO<sub>2</sub> Reduction on Graphene-Embedded Fe-N-C Motifs: Bridging Concepts Between Molecular Homogeneous and Solid-State Heterogeneous Catalysis. *ACS Energy Lett.* **2019**, *4*, 1663-1671.

- 10 Wang, C.-M.; Wang, Y.-D.; Ge, J.-W.; Xie, Z.-K. Industrial Perspective on Single-Atom Catalysis. *Chem* **2019**, *5*, 2736-2737.
- 11 Sedov, I. V.; Makhaev, V. D.; Matkovskii, P. E. Single-Site Catalysts in the Industrial Production of Polyethylene. *Catal. Ind.* **2012**, *4*, 129-140.
- 12 Yang, X.-F.; Wang, A.; Qiao, B.; Li, J.; Liu, J.; Zhang, T. Single-Atom Catalysts: A New Frontier in Heterogeneous Catalysis. *Acc. Chem. Res.* **2013**, *46*, 8, 1740-1748.
- 13 Gao, G.; Jiao, Y.; Waclawik, E. R.; Du, A. Single Atom (Pd/Pt) Supported on Graphitic Carbon Nitride as an Efficient Photocatalyst for Visible-Light Reduction of Carbon Dioxide. *J. Am. Chem. Soc.* **2016**, *138*, 6292-6297.
- 14 Wang, S.; Li, J.; Li, Q.; Bai, X.; Wang, J. Metal Single-Atom Coordinated Graphitic Carbon Nitride as an Efficient Catalyst for CO Oxidation. *Nanoscale* **2020**, *12*, 364-371.
- 15 Luo, H.; Liu, Y.; Dimitrov, S. D.; Steier, L.; Guo, S.; Li, X.; Feng, J.; Xie, F.; Fang, Y.; Sapelkin, A.; Wang, X.; Titirici, M.-M. Pt Single-Atoms Supported on Nitrogen-Doped Carbon Dots for Highly Efficient Photocatalytic Hydrogen Generation. *J. Mater. Chem. A* **2020**, *8*, 14690-14696.
- 16 Wang, Y.; Wang, X.; Antonietti, M. Polymeric Graphitic Carbon Nitride as a Heterogeneous Organocatalyst: From Photochemistry to Multipurpose Catalysis to Sustainable Chemistry. *Angew. Chem. Int. Ed.* **2012**, *51*, 68-89.
- 17 Wu, P.; Tan, S.; Moon, J.; Yan, Z.; Fung, V.; Li, N.; Yang, S.-Z.; Cheng, Y.; Abney, C. W.; Wu, Z.; Savara, A.; Momen, A. M.; Jiang, D.-e.; Su, D.; Li, H.; Zhu, W.; Dai, S.; Zhu, H. Harnessing Strong Metal-Support Interactions *via* a Reverse Route. *Nat. Commun.* **2020**, *11*, 3042.
- 18 Tauster, S. J.; Fung, S. C. Strong Metal-Support Interactions: Occurrence among the Binary Oxides of Groups IIa-Vb. *J. Catal.* **1978**, *55*, 29-35.
- 19 Ghosh, I.; Khamrai, J.; Savateev, A.; Shlapakov, N.; Antonietti, M.; Konig, B. Organic Semiconductor Photocatalyst can Bifunctionalize Arenes and Heteroarenes. *Science* **2019**, *365*, 360-366.

- 20 Pieber, B.; Malik, J. A.; Cavedon, C.; Gisbertz, S.; Savateev, A.; Cruz, D.; Heil, T.; Zhang, G.; Seeberger, P. H. Evidence for Photocatalyst Involvement in Oxidative Additions of Nickel-Catalyzed Carboxylate *O*-Arylations. *Angew. Chem. Int. Ed.* **2019**, *58*, 9575-9580.
- 21 Khamrai, J.; Ghosh, I.; Savateev, A.; Antonietti, M.; König, B. Photo-Ni-Dual-Catalytic C(sp<sup>2</sup>)-C(sp<sup>3</sup>) Cross-Coupling Reactions with Mesoporous Graphitic Carbon Nitride as a Heterogeneous Organic Semiconductor Photocatalyst. *ACS Catal.* **2020**, *10*, 3526-3532.
- 22 Cavedon, C.; Madani, A.; Seeberger, P. H.; Pieber, B. Semiheterogeneous Dual Nickel/Photocatalytic (Thio)Etherification Using Carbon Nitrides. *Org. Lett.* **2019**, *21*, 5331-5334.
- 23 Savateev, A.; Antonietti, M. Ionic Carbon Nitrides in Solar Hydrogen Production and Organic Synthesis: Exciting Chemistry and Economic Advantages. *ChemCatChem* **2019**, *11*, 6166-6176.
- 24 Lau, V. W.; Klose, D.; Kasap, H.; Podjaski, F.; Pignie, M. C.; Reisner, E.; Jeschke, G.; Lotsch, B. V. Dark Photocatalysis: Storage of Solar Energy in Carbon Nitride for Time-Delayed Hydrogen Generation. *Angew. Chem. Int. Ed.* **2017**, *56*, 510-514.
- 25 Markushyna, Y.; Smith, C. A.; Savateev, A. Organic Photocatalysis: Carbon Nitride Semiconductors vs. Molecular Catalysts. *Eur. J. Org. Chem.* **2020**, *20*, 1294-1309.
- 26 Zhang, G.; Liu, M.; Heil, T.; Zafeiratos, S.; Savateev, A.; Antonietti, M.; Wang, X. Electron Deficient Monomers that Optimize Nucleation and Enhance the Photocatalytic Redox Activity of Carbon Nitrides. *Angew. Chem. Int. Ed.* **2019**, *58*, 14950-14954.
- 27 Jiang, L.; Yuan, X.; Pan, Y.; Liang, J.; Zeng, G.; Wu, Z.; Wang, H. Doping of Graphitic Carbon Nitride for Photocatalysis: A Review. *Appl. Catal. B* **2017**, *217*, 388-406.
- 28 Yang, Y.; Guo, M.; Zhang, G.; Li, W. Tuning the Electronic and Magnetic Properties of Porous Graphene-Like Carbon Nitride Through 3d Transition-Metal Doping. *Carbon* **2017**, *117*, 120-125.

- 29 V. W.-h. Lau, I. Moudrakovski, T. Botari, S. Weinberger, M. B. Mesch, V. Duppel, J. Senker, V. Blum, B. V. Lotsch, Rational design of carbon nitride photocatalysts by identification of cyanamide defects as catalytically relevant sites. *Nat. Commun.* **2016**, *7*, 12165.
- 30 Chen, Z.; Pronkin, S.; Fellingner, T. P.; Kailasam, K.; Vilé, G.; Albani, D.; Krumeich, F.; Leary, R.; Barnard, J.; Thomas, J. M.; Perez-Ramirez, J.; Antonietti, M.; Dontsova, D. Merging Single-Atom-Dispersed Silver and Carbon Nitride to a Joint Electronic System *via* Copolymerization with Silver Tricyanomethanide. *ACS Nano* **2016**, *10*, 3166-3175.
- 31 Copéret, C. Fuels and Energy Carriers from Single-Site Catalysts Prepared *via* Surface Organometallic Chemistry. *Nat. Energy* **2019**, *4*, 1018-1024.
- 32 Sun, Y.; Silvioli, L.; Sahraie, N. R.; Ju, W.; Li, J.; Zitolo, A.; Li, S.; Bagger, A.; Arnarson, L.; Wang, X.; Moeller, T.; Bernsmeier, D.; Rossmeisl, J.; Jaouen, F.; Strasser, P. Activity-Selectivity Trends in the Electrochemical Production of Hydrogen Peroxide over Single-Site Metal-Nitrogen-Carbon Catalysts. *J. Am. Chem. Soc.* **2019**, *141*, 12372-12381.
- 33 Vilé, G. Photocatalytic Materials and Light-Driven Continuous Processes to Remove Emerging Pharmaceutical Pollutants from Water and Selectively Close the Carbon Cycle. *Catal. Sci. Technol.* **2021**, *11*, 43-61.
- 34 Silva, M.; Murzin, V.; Zhang, L.; Baltrus, J.; Baltrusaitis, J. Transition Metal-Doped MgO Nanoparticles for Nutrient Recycling: An Alternate Mg Source for Struvite Synthesis from Wastewater. *Environ. Sci.: Nano* **2020**, *7*, 3482-3496.
- 35 Chen, P.; Wang, F.; Chen, Z.-F.; Zhang, Q.; Su, Y.; Shen, L.; Yao, K.; Liu, Y.; Cai, Z.; Lv, W.; Liu, G. Study on the Photocatalytic Mechanism and Detoxicity of Gemfibrozil by a Sunlight-Driven TiO<sub>2</sub>/Carbon Dots Photocatalyst: The Significant Roles of Reactive Oxygen Species. *Appl. Catal. B* **2017**, *204*, 250-259.
- 36 Ma, J.; Lv, W.; Chen, P.; Lu, Y.; Wang, F.; Li, F.; Yao, K.; Liu, G. Aquatic Photodegradation of Clofibric Acid Under Simulated Sunlight Irradiation: Kinetics and Mechanism Analysis. *Environ. Sci. Pollut. Res. Int.* **2016**, *23*, 14294-14306.



- 37 Lanzafame, P.; Centi, G.; Perathoner, S. Catalysis for Biomass and CO<sub>2</sub> Use Through Solar Energy: Opening New Scenarios for a Sustainable and Low-Carbon Chemical Production. *Chem. Soc. Rev.* **2014**, *43*, 7562-7580.
- 38 Heck, K. N.; Garcia-Segura, S.; Westerhoff, P.; Wong, M. S. Catalytic Converters for Water Treatment. *Acc. Chem. Res.* **2019**, *52*, 906-915.
- 39 Lakhi, K. S.; Park, D. H.; Al-Bahily, K.; Cha, W.; Viswanathan, B.; Choy, J. H.; Vinu, A. Mesoporous Carbon Nitrides: Synthesis, Functionalization, and Applications. *Chem. Soc. Rev.* **2017**, *46*, 72-101.
- 40 Jin, X.; Wang, R.; Zhang, L.; Si, R.; Shen, M.; Wang, M.; Tian, J.; Shi, J.; Electron Configuration Modulation of Nickel Single Atoms for Elevated Photocatalytic Hydrogen Evolution. *Angew. Chem. Int. Ed.* **2020**, *59*, 6827-6831.
- 41 Liu, H.; Chen, D.; Wang, Z.; Jing, H.; Zhang, R. Microwave-Assisted Molten-Salt Rapid Synthesis of Isotype Triazine-/Heptazine Based g-C<sub>3</sub>N<sub>4</sub> Heterojunctions with Highly Enhanced Photocatalytic Hydrogen Evolution Performance. *Appl. Catal. B* **2017**, *203*, 300-313.
- 42 Fang, D.; He, F.; Xie, J.; Xue, L. Calibration of Binding Energy Positions with C1s for XPS Results. *J. Wuhan Univ. Technol. Mater. Sci. Ed.* **2020**, *35*, 711-718.
- 43 Lin, Z.; Wang, X. Nanostructure Engineering and Doping of Conjugated Carbon Nitride Semiconductors for Hydrogen Photosynthesis. *Angew. Chem. Int. Ed.* **2013**, *52*, 1735-1738.
- 44 Due to low Cu content in CuI@mpg-C<sub>3</sub>N<sub>4</sub>, shift of C<sub>carb</sub> peak in XPS C 1s is not observed.
- 45 Wang, J.; Heil, T.; Zhu, B.; Tung, C.-W.; Yu, J.; Chen, H. M.; Antonietti, M.; Cao, S. A Single Cu-Center Containing Enzyme-Mimic Enabling Full Photosynthesis under CO<sub>2</sub> Reduction. *ACS Nano* **2020**, *14*, 8584-8593.
- 46 Yang, P.; Zuo, S.; Zhang, F.; Yu, B.; Guo, S.; Yu, X.; Zhao, Y.; Zhang, J.; Liu, Z. Carbon Nitride-Based Single-Atom Cu Catalysts for Highly Efficient Carboxylation of Alkynes with Atmospheric CO<sub>2</sub>. *Ind. Eng. Chem. Res.* **2020**, *59*, 7327-7335.

- 47 Yang, Y.; Wang, C.; Gao, S.; Mao, K.; Xia, G.; Lin, Z.; Jiang, P.; Hu, L.; Chen, Q. Incorporation of Cu-N<sub>x</sub> Cofactors into Graphene Encapsulated Co as Biomimetic Electrocatalysts for Efficient Oxygen Reduction. *Nanoscale* **2018**, *10*, 21076-21086.
- 48 Wu, H.; Li, H.; Zhao, X.; Liu, Q.; Wang, J.; Xiao, J.; Xie, S.; Si, R.; Yang, F.; Miao, S.; Guo, X.; Wang, G.; Bao, X. Highly Doped and Exposed Cu(I)-N Active Sites within Graphene Towards Efficient Oxygen Reduction for Zinc-Air Batteries. *Energy Environ. Sci.* **2016**, *9*, 3736-3745.
- 49 Zhang, J.; Guo, F.; Wang, X. An Optimized and General Synthetic Strategy for Fabrication of Polymeric Carbon Nitride Nanoarchitectures. *Adv. Funct. Mater.* **2013**, *23*, 3008-3014.
- 50 Maeda, K.; Kuriki, R.; Zhang, M.; Wang, X.; Ishitani, O. The Effect of the Pore-Wall Structure of Carbon Nitride on Photocatalytic CO<sub>2</sub> Reduction under Visible Light. *J. Mater. Chem. A* **2014**, *2*, 15146-15151.
- 51 Typically, fluorescence quenching experiments are performed in solution. Therefore, Stern-Volmer constant is expressed in mol<sup>-1</sup> L<sup>-1</sup>. In this work we investigate semiconductor material modified with metal single atoms. It is more appropriate to use quencher (metal single atoms) concentration expressed in wt.% (data obtained from the elemental analysis).
- 52 Romero, N. A.; Nicewicz, D. A. Organic Photoredox Catalysis. *Chem. Rev.* **2016**, *116*, 10075-10166.
- 53 Given that emission of a photon by fluorophore is a statistic process with the probability falling exponentially over the time, Cu single atoms quench the most efficiently excitons with longer lifetime.
- 54 Kisch, H. Semiconductor Photocatalysis-Mechanistic and Synthetic Aspects. *Angew. Chem. Int. Ed.* **2013**, *52*, 812-847.
- 55 We presume that in Ag1@mpg-C<sub>3</sub>N<sub>4</sub> having lower surface area compared to Ag2@mpg-C<sub>3</sub>N<sub>4</sub>, substantial fraction of metal single atoms is located in the bulk of the material.

- 56 Karthikeyan, S.; Dionysiou, D. D.; Lee, A. F.; Suvitha, S.; Maharaja, P.; Wilson, K.; Sekaran, G. Hydroxyl Radical Generation by Cactus-Like Copper Oxide Nanoporous Carbon Catalysts for Microcystin-LR Environmental Remediation. *Catal. Sci. Technol.* **2016**, *6*, 530-544.
- 57 Cho, Y. J.; Kim, S. Y.; Cho, M.; Wee, K. R.; Son, H. J.; Han, W. S.; Cho, D. W.; Kang, S. O. Ligand-To-Ligand Charge Transfer in Heteroleptic Ir-Complexes: Comprehensive Investigations of its Fast Dynamics and Mechanism. *Phys. Chem. Chem. Phys.* **2016**, *18*, 15162-15169.
- 58 Vogler, A.; Kunkely, H. Ligand-To-Ligand and Intraligand Charge Transfer and their Relation to Charge Transfer Interactions in Organic Zwitterions. *Coord. Chem. Rev.* **2007**, *251*, 577-583.
- 59 La Porte, N. T.; Martinez, J. F.; Hedström, S.; Rudshiteyn, B.; Phelan, B. T.; Mauck, C. M.; Young, R. M.; Batista, V. S.; Wasielewski, M. R. Photoinduced Electron Transfer from Rylenediimide Radical Anions and Dianions to  $\text{Re}(\text{bpy})(\text{CO})_3$  Using Red and Near-Infrared Light. *Chem. Sci.* **2017**, *8*, 3821-3831.
- 60 Gomez Cortes, L.; Marinov, D.; Sanseverino, I.; Navarro Cuenca, A.; Niegowska, M.; Porcel Rodriguez, E.; Lettieri, T. Selection of Substances for the 3rd Watch List under the Water Framework Directive, EUR 30297EN, Publications Office of the European Union, Luxembourg, **2020**, ISBN 978-92-76-19426-2.
- 61  $\text{CO}_2$  is the thermodynamically stable product from the selective degradation of Gemfibrozil and ideally it can be recovered to make fuels, chemicals, and drugs. An incomplete degradation of Gemfibrozil can lead to the generation of toxic byproducts. By designing single-atom catalysts based on mpg- $\text{C}_3\text{N}_4$ , this work shows that it is possible to reduce the content of organic species, leading to an increased selectivity to  $\text{CO}_2$ . The result can be correlated with the content of ionic metal species in the samples.
- 62 Yu, H.; Nie, E.; Xu, J.; Yan, S.; Cooper, W. J.; Song, W. Degradation of Diclofenac by Advanced Oxidation and Reduction Processes: Kinetic Studies, Degradation Pathways and Toxicity Assessments. *Water Res.* **2013**, *47*, 1909-1918.

- 63 Liu, D.; Jin, C.; Shan, F.; He, J.; Wang, F. Synthesizing BaTiO<sub>3</sub> Nanostructures to Explore Morphological Influence, Kinetics, and Mechanism of Piezocatalytic Dye Degradation. *ACS Appl. Mater. Interfaces* **2020**, *12*, 17443-17451.
- 64 Zhao, Y.; Antonietti, M. Visible-Light-Irradiated Graphitic Carbon Nitride Photocatalyzed Diels-Alder Reactions with Dioxygen as Sustainable Mediator for Photoinduced Electrons. *Angew. Chem. Int. Ed.* **2017**, *56*, 9336-9340.
- 65 Su, F.; Mathew, S. C.; Lipner, G.; Fu, X.; Antonietti, M.; Blechert, S.; Wang, X. Mpg-C<sub>3</sub>N<sub>4</sub>-Catalyzed Selective Oxidation of Alcohols Using O<sub>2</sub> and Visible Light. *J. Am. Chem. Soc.* **2010**, *132*, 16299-16301.
- 66 Su, F.; Mathew, S. C.; Möhlmann, L.; Antonietti, M.; Wang, X.; Blechert, S. Aerobic Oxidative Coupling of Amines by Carbon Nitride Photocatalysis with Visible Light. *Angew. Chem. Int. Ed.* **2011**, *50*, 657-660.

# Graphical Abstract

